

DEM Analysis of Sandbox Experiments on Strike-slip Faulting



H. Taniyama

Saitama University, Japan

SUMMARY

A distinct element method analysis was carried out to examine the development of shear bands observed in sandbox experiments on strike-slip faulting. The analysis reproduced shear bands typically observed in sandbox experiments. It was shown that simple shear in the horizontal plane and the stress due to dilatancy account for the formation of shears that have a 'cirque' or 'shell' or 'ship body' shape. Drag due to the dependence of velocity on depth and simple shear in the horizontal plane are confirmed to control the helicoidal shape of Riedel shears. It was observed that the compressional direction in the region enclosed with Riedel shears is at a lower angle to the basement fault than the compressional direction outside of the Riedel shears and that shears in the deep part of the sandbox model formed at a smaller interval than shears in the shallow part.

Keywords: Strike-slip fault, Surface fault rupture, Distinct element method

1. INTRODUCTION

Overburden soil beds overlying a fault are often deformed by propagation of earthquake rupture. This coseismic faulting often causes damage to structures. To mitigate such damage, it is important to understand the behaviour of overlying deposits during the displacement of the underlying bedrock. En echelon Riedel shears (Fig. 1(a)), lower-angle shears and P shears (Fig. 1(b)) are commonly observed when overburden deposits are subjected to strike-slip faulting. Splay faults and antithetic Riedel shears are sometimes observed during the process. For example, Tchalenko and Ambraseys (1970) examined fractures associated with the Dasht-e Bayaz earthquake, Iran. Although the complexity of the fractures varied from place to place depending on the development of Riedel shears, P shears and antithetic Riedel shears, they showed that a simple shear deformation model based on the Coulomb failure criterion could account for most of the observed structures. Development of shear bands due to strike slip has been examined experimentally by several authors (e.g., Tchalenko, 1970, Wilcox et al., 1973). Naylor et al. (1986) performed scaled sandbox experiments to generate models for relative ages, dip, strike and three-dimensional shape of faults in basement-controlled wrench faulting. They showed the helicoidal geometry of Riedel shears in a sandbox from vertical and horizontal serial sections. They also showed that the initial stress conditions affected the shape of Riedel shears. Ueta et al. (2000) applied computerized X-ray tomography to sandbox experiments and analyzed the kinematic evolution of the shear bands caused by strike-slip faulting. They found that the evolution of shear bands in the model sand is as follows. (1) Right-stepping shears that have a 'cirque' or 'shell' or 'ship body' shape develop on both sides of the basement fault. (2) The shears on one side of the basement fault join those of the other side, forming a helicoidal shape of Riedel shear. (3) Lower-angle shears and P shears, which have steeper dips and a less pronounced helicoidal aspect than Riedel shears, develop within the zone defined by the first Riedels.

In this study, a distinct element method analysis was carried out to examine the development of shear bands observed in sandbox experiments on strike-slip faulting.



Figure 1. (a) Riedel shears, (b) lower-angle shears and P shears

2. NUMERICAL MODELING

About 880000 spherical elements (37 percent of particles have a diameter of 3 mm, 45 percent have a diameter of 4 mm and 18 percent have a diameter of 5 mm) are used to model the sandbox. The basement and side walls are made of 3 mm diameter spheres and assumed to be rigid. Periodic boundary conditions are imposed at boundaries in the strike direction and if an element goes beyond the boundary it is placed at the opposite boundary. The elements are air pluviated into the box. The frictional coefficient is set to zero to prepare the initial sedimentary model. The length (x direction) and the width (y direction) of the sandbox model is 57.6 cm and 35.1 cm respectively. The height of the sandbox model after the preparation process is 21.5 cm (Fig. 2). Parameters used in the analysis are shown in Table 1.

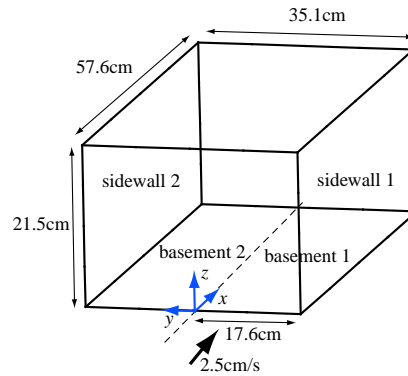


Figure 2. Sandbox model

Table 1. Parameters of the analysis

Diameter of particles	3mm, 4mm, 5mm
Number of particles	887965
Density of particles	2400kg/m ³
Normal spring constant	1.0 × 10 ⁵ N/m
Tangential spring constant	3.0 × 10 ⁴ N/m
Normal damping coefficient	0.80 Ns/m
Tangential damping coefficient	0.44 Ns/m
Coefficient of friction	0.5

Iwashita and Oda (1998) took rolling resistance at contacts into account in DEM analysis and showed the importance of rolling in forming shear bands. They included an additional spring and dashpot at each contact to simulate the relation between the moment and the roll and rolling rate of particles. The rolling stiffness k_r was given as the product of the tangential spring constant k_s and the square of the radius, on the assumption that a moment due to the sliding displacement dU_s and a moment due to the rolling displacement dU_r are the same order of magnitude under the condition of $dU_s \approx dU_r$. In the present study, we use spherical elements with normal, shear and rolling springs and normal and shear dashpots. A moment at a contact is calculated in the same way as Iwashita and Oda (1998). A normal force acts only when there is an overlap at the contacts between the elements and the effects of tension are not considered. The maximum shear force (F_{\max}) and moment (M_{\max}) are described as follows.

$$F_{\max} = \mu F_n \quad (2.1)$$

$$M_{\max} = \alpha BF_n \quad (2.2)$$

where F_n is the (compressional) normal force, μ is the frictional coefficient, B is the length of contact area and α is a parameter which determines the rolling resistance and assumed to be 5.0. If the absolute value of the shear force or moment is larger than F_{\max} or M_{\max} , it is set equal to F_{\max} or M_{\max} , respectively.

The basement is divided into two halves at $y=0$. One of the divided basement and side wall (basement 2 and side wall 2 in Fig. 2) are fixed and the other basement and side wall (basement 1 and side wall 1 in Fig. 2) move in the $+x$ direction at 2.5 cm/s.

3. RESULTS AND DISCUSSION

3.1. Deformation at the Ground Surface

Fig. 3 shows the deformation at the ground surface when the basement fault displacement is 2 cm (Fig. 3(a)), 4.6 cm (Fig. 3(b)), 6 cm (Fig. 3(c)) and 10 cm (Fig. 3(d)). Deformation of particles initially located on the 2.4 cm grid is shown. Shear strain (γ_{xy}) or shear strain increment ($\Delta\gamma_{xy}$) distribution at the height of 21 cm is also shown and white zones enclosed with red lines indicate high strain (strain increment) zones. The dotted line on the right side indicates the location of the basement fault line.

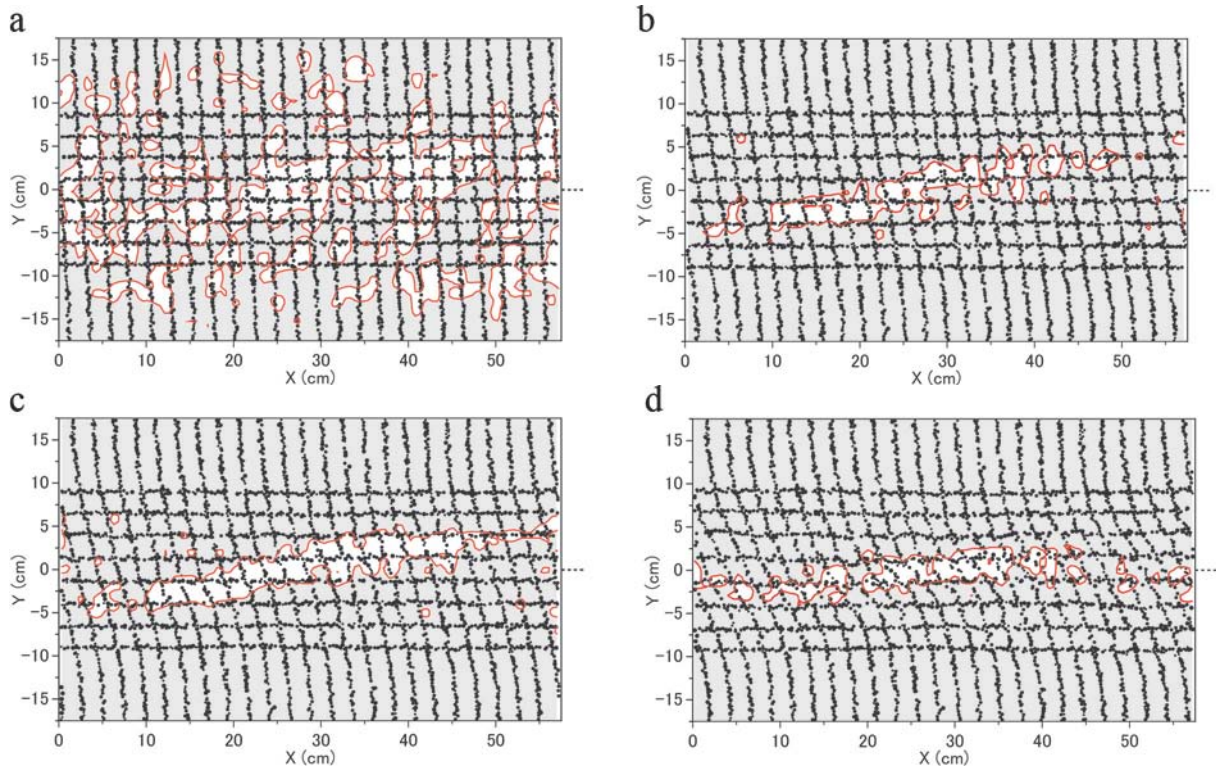


Figure 3. Particle deformation at the ground, for a basement displacement of (a) 2.0 cm, (b) 4.6 cm, (c) 6.0 cm and (d) 10.0 cm. White zones enclosed with red lines indicate high strain (increment) area where the shear strain increment $\Delta\gamma_{xy}$ exceeds (a) 0.07 for a basement displacement of 0–2cm, (b) 0.045 for a basement displacement of 4.0–4.6cm, (c) 0.08 for a basement displacement of 5.0–6.0cm and (d) 0.11 for a basement displacement of 9.0–10.0 cm.

Surface feature when the basement displacement is 2 cm shows general distortion and strain localization is not observed (Fig. 3(a)).

High strain zones which transversely cross the basement fault line are observed as the basement displacement exceeds 4 cm. In Fig. 3(b) white zones enclosed with red lines ($\Delta\gamma_{xy}$ during the basement displacement from 4.0cm to 4.6cm is 0.045 or larger) strike at about 15° to the basement fault line. The location of the high strain zone is almost the same until the basement displacement is 6 cm (Fig. 3(c)). Because periodic boundary conditions are imposed at boundaries in the strike direction, an echelon high strain zones are formed at an interval of 57.6 cm (model length). The high strain zone in Fig. 3(b) and 3(c) is considered to be Riedel shear. The strike angle of 15° is smaller than that of Oyama and Tani (2003) ($18\text{--}33^\circ$) and in reasonable agreement with Naylor et al. (1986) (average 17°), Tchhalenko (1970) ($12 \pm 1^\circ$ and 16° after rotation) and Ueta et al. (2000) ($14\text{--}23^\circ$ for loose sand). The basement fault displacements of 4.0 cm and 4.6 cm, which correspond to 0.19 and 0.21 times the model thickness, are compatible with the displacement necessary to propagate to the ground for thin sand sediment (Oyama and Tani, 2003).

When the basement fault displacement exceeds 6 cm, large deformation occurs near the basement fault line. Deformation of particles when the basement fault displacement is 10 cm and shear strain increment during the basement displacement from 9.0 cm to 10.0 cm (Fig. 3(d)) show high strain zones trending at low angle ($7\text{--}8^\circ$) to the basement fault. Oyama and Tani (2003) observed that lower angle shears and the basement fault strike at $5\text{--}15^\circ$ and that the basement fault displacement 1.5 to 2.3 times the one for Riedel shears is necessary for lower angle shears to propagate to the ground. The secondarily formed lower angle high strain increment zone is considered to be lower angle shear.

3.2. Deformation and Stress in the Sandbox Model

3.2.1. First shears

Isosurface of maximum strain increment of 0.07 for a basement displacement of 0.4–1.0 cm is shown in Fig. 4 High strain zones are observed near the basement fault line at the bottom of the model and extend obliquely upward on both sides of the basement fault line. Fig. 5 shows the isosurface of maximum strain increment of 0.11 for a basement displacement of 1.6–2.2 cm.

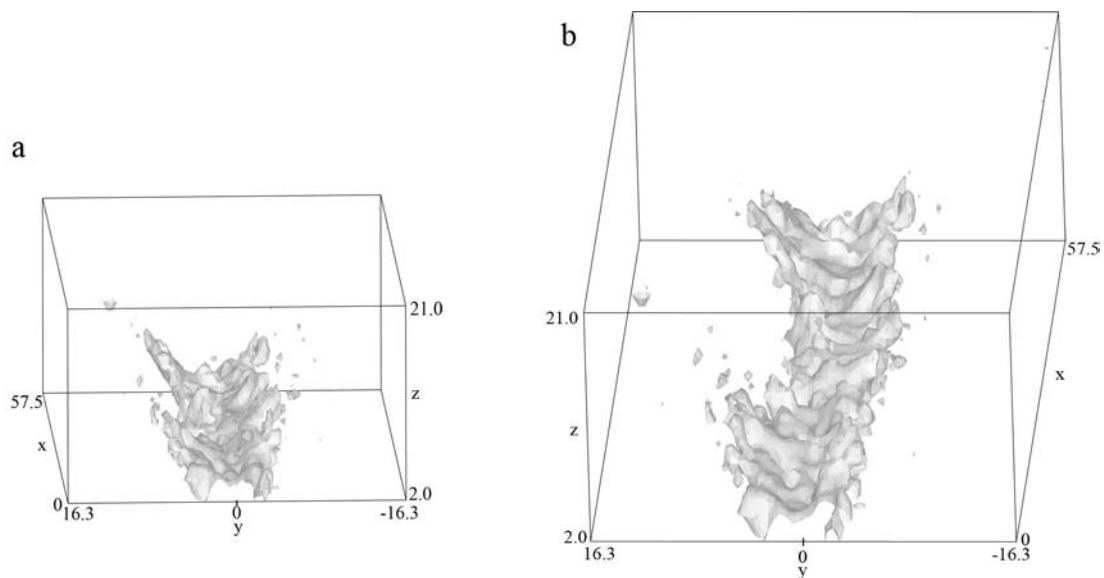


Figure 4. Three-dimensional plot of high-strain-increment zone. Isosurface of maximum strain increment ($\Delta\gamma_{\max}$) of 0.07 for a basement displacement of 0.4–1.0 cm is shown. (a) and (b) are viewed from other angles.

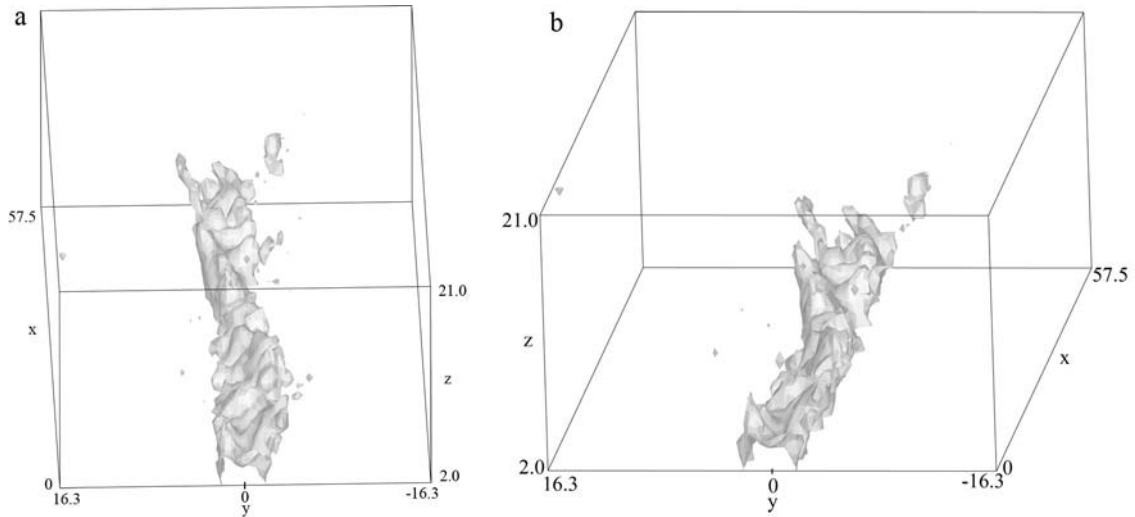


Figure 5. Three-dimensional plot of high-strain-increment zone. Isosurface of maximum strain increment ($\Delta\gamma_{\max}$) of 0.11 for a basement displacement of 1.6–2.2 cm is shown. (a) and (b) are viewed from other angles.

With the increase of basement displacement, strain in the shallow part of the model increases but the most significantly deformed zone extends transversely to the basement fault. Shears that have a ‘cirque’ or ‘shell’ or ‘ship body’ shape develop on both sides of the basement fault at the earliest stage of deformation and the shears on one side of the basement fault join those on the other side and each shear surface forms a helicoidal shape (Ueta et al., 2000). The high strain zones in Fig. 4 and Fig. 5 are similar to shears observed in sandbox experiments both in shape and process of development and are interpreted to correspond to those shears.

Horizontal deformation of sandbox is simple shear deformation and the horizontal stress at 45° to the basement fault is the maximum compressive stress in the horizontal plane (Fig. 6). This stress state cannot account for the formation of shears observed in the early stage of deformation. The stresses in the subsurface will differ from these because of the vertical component of stresses. The maximum compressive stress orientation in a vertical plane for $x=20\text{cm}$ with a basement fault displacement of 6 mm is shown in Fig. 7. Fig. 8 shows particle movements in the same plane. Quintupled particle movements during the basement displacement from 0 to 6 mm are shown. Because of the dilatancy due to shear deformation, particles move outward from the basement fault (Fig. 8). Accordingly the maximum compressive orientation dips toward the basement fault except in the lowest part of the model (Fig. 7). The maximum compressive orientation in xy plane has a bottom-left to upper-right direction (Fig. 6). The maximum compressive orientation in yz plane has a upper-left to bottom-right direction in $y<0$. The minimum compressive orientation has an opposite sense direction. Shear failure surface under this stress state ($45^\circ - \phi/2$ to the maximum compressive stress orientation and $45^\circ + \phi/2$ to the minimum compressive stress orientation, where ϕ is the friction angle) is shown in Fig. 9. x' , y' and z' in Fig. 9 are taken parallel to x , y and z axes. Dotted part of the line is behind the failure surface and thin-colored part of the line is in $z'<0$. The failure surface is parallel or strikes at a very low angle to x (x') axis. Because of the antisymmetry of the vertical stress with respect to $y=0$, the failure surface in $y>0$ has a shape rotated 180° with respect to z axis. Simple shear in the horizontal plane and the stress due to dilatancy form shears that have a ‘cirque’ or ‘shell’ or ‘ship body’ shape.

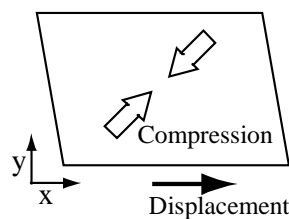


Figure 6. Deformation and compressive direction in the horizontal plane

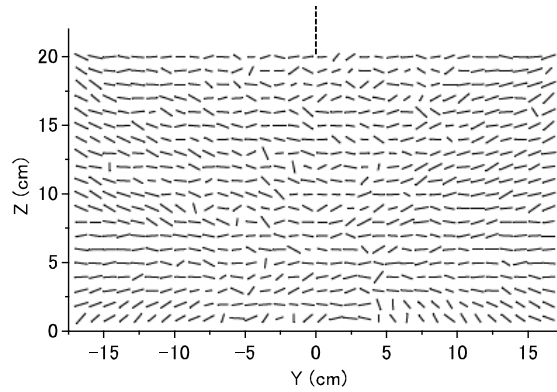


Figure 7. Maximum principal-stress (compressive) direction in the vertical plane for $x=20$ cm with a basement displacement of 6 mm

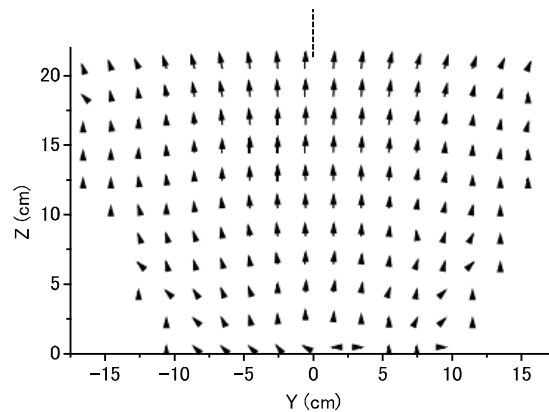


Figure 8. Quintupled particle movements in the vertical plane for $x=20$ cm during the basement displacement from 0 to 6 mm

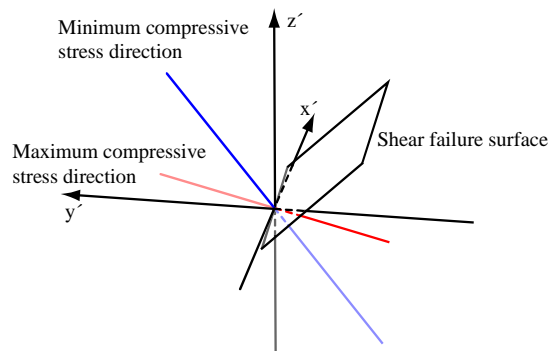


Figure 9. Maximum and minimum compressive stress direction and shear failure surface when the effect of dilation is large

The deformation concentrates near the basement fault at the bottom of the sandbox whereas it spreads over a wider area near the surface (Fig. 10). Particles in the deep part of the sandbox move faster in the strike direction than particles in the shallow part, especially near the basement fault line. Thus, velocity (slip) in the strike direction differs with height even if the horizontal distance from the basement fault is the same. This velocity difference with respect to height, referred to as “drag” in Naylor et al. (1986), causes the compressive stress shown in Fig. 11, which is antisymmetric with respect to the basement-fault line. This effect becomes large at a relatively developed stage of deformation when the velocity difference with respect to height is large. Shear failure surface under the stress state as shown in Fig. 6 and Fig. 11 is schematically shown in Fig. 12. x' , y' and z' in Fig. 12 are taken parallel to x , y and z axes. Failure surface transversely crosses the x' axis and inclines toward

$-y'$ direction. Because of the antisymmetric deformation in xz plane with respect to $y=0$, failure surface on the opposite side of the basement fault has a shape rotated 180° with respect to z axis. Failure surface at $y=0$ is vertical. Simple shear in the horizontal plane and the velocity difference with respect to height give rise to the formation of helicoidally shaped shears.

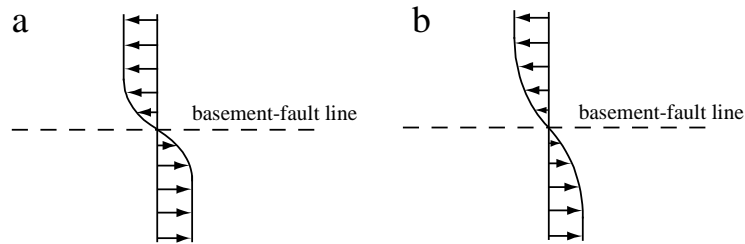


Figure 10. Schematic showing deformation and particle movement in (a) deep part and (b) shallow part

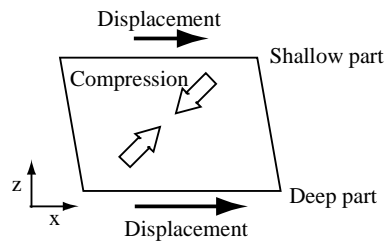


Figure 11. Deformation and compressive direction in the vertical (xz) plane

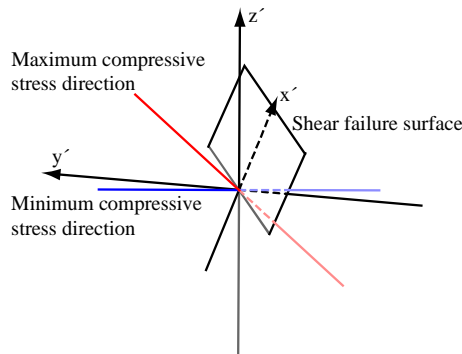


Figure 12. Maximum and minimum compressive stress direction and shear failure surface when the effect of velocity difference is large

3.2.2. Deformation in the deep part of the sandbox model

Strain increment distribution in the deep part of the model at the early stage of deformation is shown in Fig. 13, Fig. 14 and Fig. 15. In the strain increment distribution at heights of 4 cm and 10 cm, development of a high strain increment zone which transversely crosses the basement fault line is observed. This high strain increment zone corresponds to the first shear and has an interval of 57.6 cm because of the cyclic condition. The maximum shear strain increment distribution at the height of 2.0 cm and at the early stage of deformation (Fig. 13(c)) shows a few zones of linear strain concentration which transversely cross the basement fault line at about $x=10\text{cm}$, $x=20\text{cm}$, $x=30\text{cm}$ and $x=40\text{--}50\text{cm}$. Only the high strain increment zone around $x=30\text{cm}$ continues to develop (Fig. 14(c)) and form the first shear. At the height of 4 cm, strain increment around the basement fault ($y=0$) is relatively large at about $x=10\text{cm}$ and $x=50\text{cm}$, although the main deformation occurs in the high strain increment zone corresponding to the first shear. At the height of 10 cm, large deformation is not observed either at around $x=10\text{cm}$ and $y=0\text{cm}$ or $x=50\text{cm}$ and $y=0\text{cm}$. Oyama and Tani (2003) observed that the interval of Riedel shears formed in the sandbox is an integral multiple of the interval of shears that have a ‘cirque’ or ‘shell’ or ‘ship body’ shape. They also observed that a fraction of shears that have a ‘cirque’ or ‘shell’ or ‘ship body’ shape develop to form Riedel shear. The result of this DEM analysis

suggests that only some of the shears which form in the deep part of the sediment continue to develop as they evolve toward the surface and that shears peculiar to the sediment thickness preferentially develop.

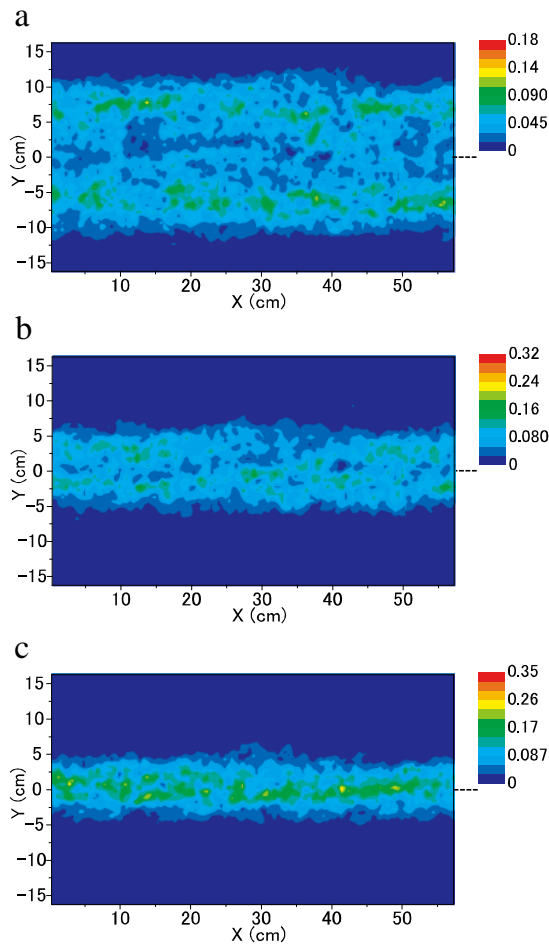


Figure 13. Maximum shear strain increment distribution for a basement displacement of 0.4–1.0 cm at heights of (a) 10 cm, (b) 4 cm and (c) 2 cm

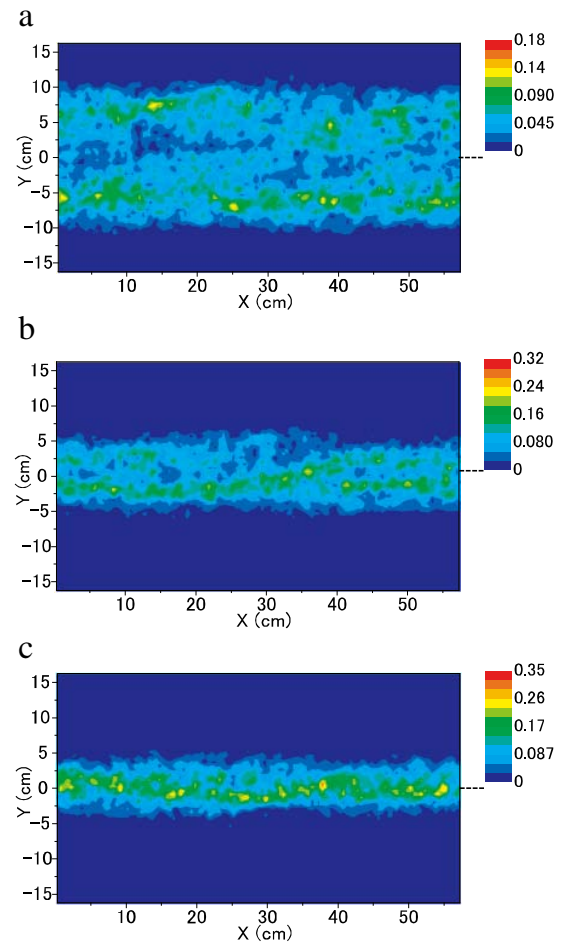


Figure 14. Maximum shear strain increment distribution for a basement displacement of 1.0–1.6 cm at heights of (a) 10 cm, (b) 4 cm and (c) 2 cm

3.2.3. After formation of first shears

First shears change the initial stress field. Around two stepping Riedel shears, stresses in the horizontal plane will be reoriented as indicated schematically in Fig. 16 (Vallejo and Shettima, 1996, Naylor et al., 1986). The maximum stress orientation and strain increment distribution after the formation of first shears are shown in Fig. 17. The x and y components of the maximum stress orientation at the height of 14 cm when the basement displacement is 4.0 cm is shown along with the maximum shear strain increment at the height of 14 cm for a basement displacement of 3.4–4.0 cm. The maximum shear strain increment in the light gray area and in the dark gray area is greater than 0.05 and 0.1 respectively. Compressional direction striking at a lower angle to the basement fault is noticeable between the high-strain-increment zones and the average striking angle in the zones enclosed with red lines in Fig. 17 is 37° . On the other hand compressional direction striking at a higher angle to the basement fault is observable outside of the high-strain-increment zones and the average striking angle in the zones enclosed with blue lines in Fig. 17 is 49° . Similar stress and strain increment distribution pattern (lower-angle compressional direction between the high-strain-increment zones and higher-angle compressional direction outside of the high-strain-increment zones) is observed at other heights. Particle movements along the high strain increment zone changes the stress field as shown in Fig. 17 and the lower-angle compressional direction in regions enclosed with high strain increment zones causes the formation of lower-angle shears which strike at a lower angle to the basement-fault

line.

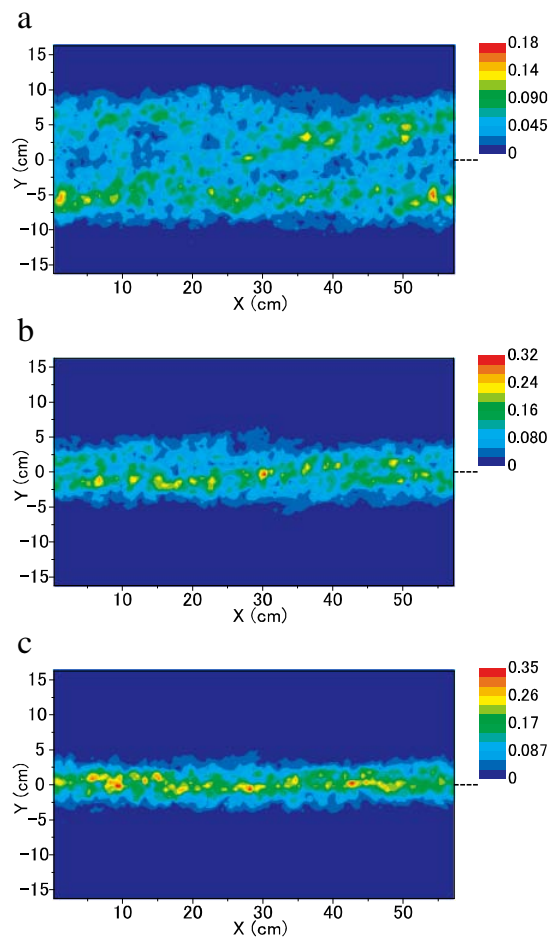


Figure 15. Maximum shear strain increment distribution for a basement displacement of 1.6–2.2 cm at heights of (a) 10cm, (b) 4cm and (c) 2cm

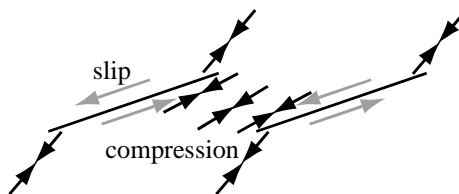


Figure 16. Rotation of compressional direction (black arrows) due to slip along Riedel shears (gray arrows)

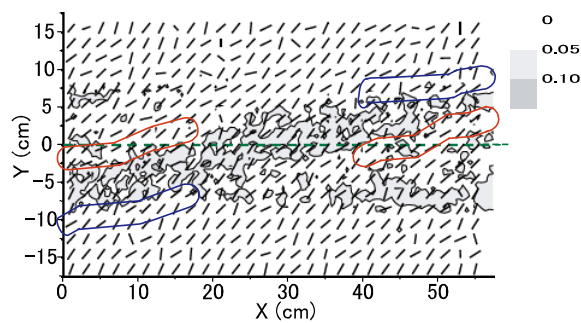


Figure 17. Maximum compressive stress direction (x and y component) for a basement displacement of 4.0 cm and maximum shear strain increment distribution for a basement displacement of 3.4–4.0 cm at a height of 14 cm

4. CONCLUSIONS

A distinct element method analysis was carried out to examine the development of shear bands observed in sandbox experiments on strike-slip faulting. The analysis reproduced shear bands typically observed in sandbox experiments such as shears that have a 'cirque' or 'shell' or 'ship body' shape, en echelon Riedel shears and lower-angle Riedel shears. It was shown that simple shear in the horizontal plane and the stress due to dilatancy account for the formation of shears that have a 'cirque' or 'shell' or 'ship body' shape. The deformation concentrates near the basement fault at the bottom of the sandbox whereas it spreads over a wider area near the surface and particles in the deep part of the sandbox move faster in the strike direction than particles in the shallow part. Drag due to this dependence of velocity on depth and simple shear in the horizontal plane are confirmed to control the helicoidal shape of Riedel shears. It was observed that the compressional direction in the region enclosed with Riedel shears is at a lower angle to the basement fault than the compressional direction outside of the Riedel shears as a result of slip along Riedel shears and that compressional direction at a low angle to the basement fault produces secondary lower-angle shears that strike at a lower angle to the basement fault and are less helicoidal in shape. Shears in the deep part of the sandbox model formed at a smaller interval than shears in the shallow part, suggesting that only some of the shears which form in the deep part of the sediment continue to develop as they evolve toward the surface and that shears peculiar to the sediment thickness preferentially develop.

ACKNOWLEDGEMENT

In this study, the computer facilities of the Earthquake Information Center of the Earthquake Research Institute, the University of Tokyo, were used.

REFERENCES

- Iwashita, K. and Oda, M. (1998). Rolling resistance at contacts in simulation of shear band development by DEM, *Journal of Engineering Mechanics. ASCE* **124:3**, 285–292.
- Naylor, M.A., Mandl, G. and Sijpesteijn, C.H.K. (1986). Fault geometries in basement-induced wrench faulting under different initial stress states. *Journal of Structural Geology* **8:7**, 737–752.
- Oyama, Y. and Tani, K. (2003). Analysis of shear band structure developed on surface of sand layer observed in strike-slip fault model tests. *JSCE* **750/III-65**, 171–181.
- Tchalenko, J.S. (1970). Similarities between shear zones of different magnitudes. *Geological Society of America Bulletin* **81**, 1625–1640.
- Tchalenko, J.S. and Ambraseys, N.N. (1970). Structural analysis of the Dasht-e Bayaz (Iran) earthquake fractures. *Geological Society of America Bulletin* **81**, 41–60.
- Ueta, K., Tani, K. and Kato, T. (2000). Computerized X-ray tomography analysis of three-dimensional fault geometries in basement-induced wrench faulting. *Engineering Geology* **56**, 197–210.
- Vallejo, L.E. and Shettima, M. (1996). Fault movement and its impact on ground deformations and engineering structures. *Engineering Geology* **43**, 119–133.
- Wilcox, R.E., Harding, T.P. and Seely, D.R. (1973). Basic wrench tectonics. *The American Association of Petroleum Geologists Bulletin* **57:1**, 74–96.